






Toroidal coupling in the kinetic response to edge magnetic perturbations

G. Spizzo¹, M. Agostini¹, P. Scarin¹, R.B. White², O. Schmitz³,
M. Spolaore¹, D. Terranova¹, M. Veranda¹ and N. Vianello¹

¹ Consorzio RFX (CNR, ENEA, INFN, Università di Padova, Acciaierie Venete SpA)
Corso Stati Uniti 4 - 35127 Padova, Italy

² Plasma Physics Laboratory, Princeton University, PO Box 451, Princeton, NJ 08543,
United States of America

³ Department of Engineering Physics, University of Wisconsin, Madison, WI 53706,
United States of America

E-mail: gianluca.spizzo@igi.cnr.it

Received 13 July 2017

Accepted for publication 6 September 2017

Published 26 October 2017



Abstract

The magnetic topology of the stochastic edge of a helical reversed-field pinch, with helicity m/n , shows to be deeply influenced by higher harmonics $(m \pm 1)/n$, with the same n , due to toroidal coupling. As a consequence, by measuring kinetic quantities in a particular θ, ϕ location, one can incur in substantial errors or mis-interpretations of the kinetic plasma response: only a full 3D coverage of θ, ϕ angles can reveal the real topology of the plasma. This can be a caveat for MP application in tokamaks, because it shows that toroidal and poloidal sidebands, though smaller than the base mode by a factor $\sim \epsilon = a/R$, can have a sizable effect on the kinetic response of the edge plasma, and thus on related issues (for example, ELM stabilization and suppression).

Keywords: tokamaks, chaos, magnetic islands, magnetic perturbations

(Some figures may appear in colour only in the online journal)

1. Introduction

Magnetic perturbations (MP) are induced in tokamaks to stabilize the edge plasma with respect to edge-localized modes (ELMs) and enhance plasma exhaust (see [1] and references therein). The method is effective, especially at low collisionality, but it induces serious drawbacks, such as the so-called ‘density pumpout’ [2] (a decrease of electron density throughout the plasma cross-section), and a series of modifications of plasma edge kinetic quantities, which have been recorded in TEXTOR [3, 4], in DIII-D [5] and, more recently, in a detailed study of ECE electron temperature profiles with the $m/n = 2/1$ MP in ASDEX Upgrade [6]. These modifications include significant perturbations of floating potential, edge electron pressure and $\vec{E} \times \vec{B}$ flow, which at a first approximation follow the helicity of the applied base mode. This is a problem with MPs, since ELM stability depends on *plasma pressure*, whereas the external knobs are the currents in the feedback coils. This mismatch between external, magnetic

action, and internal kinetic response from the plasma is a crucial problem with MPs.

In this paper we will present new results in the RFX reversed-field pinch, showing that sidebands, toroidally coupled to the base mode, complicate the kinetic plasma response to MPs. RFX possesses a different magnetic configuration with respect to tokamaks: nevertheless, it shows a stochastic edge produced by MPs which are well-controlled (in phase and amplitude) by a full coverage of 192 feedback coils. Moreover, the kinetic plasma response is measured by means of an almost full coverage (in both toroidal and poloidal angles) of edge diagnostics. This makes RFX an ideal experimental benchmark for comparing in a detailed way the action (coils) and response (kinetic quantities). Measurements will be compared to guiding-center simulations with the code ORBIT [7]: besides a more traditional interpretation in terms of connection lengths, the role of sidebands will be validated via calculations of the Poincaré recurrence time, applied for the first time to plasma physics.

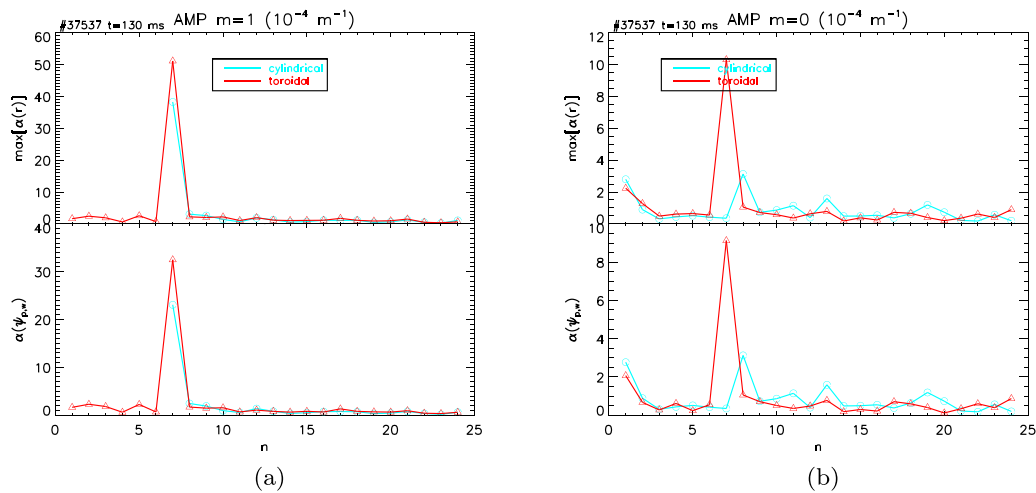


Figure 1. Spectrum of tearing modes in the RFX-mod experiment: (a) $m = 1$ modes, (b) $m = 0$ modes. Top row, maximum of the eigenfunction along the radius, bottom row, eigenfunction evaluated at the liner. In cyan, the eigenfunction is calculated in cylindrical approximation; in red, in toroidal geometry.

In previous RFX studies, a very good agreement was found between a helical $1/7$ edge topology and measurements of floating potential, edge electron pressure and $\vec{E} \times \vec{B}$ flow [8–15]: the conclusion was that plasma kinetic quantities are indeed shaped as the $1/7$ dominant helix. The theoretical reason for this is that electrons follow closely the magnetic field lines, so that even a small amount of chaos can influence electron density and temperature [16–19]. The effect on the floating potential is more subtle, and a proposed theory involves the role of ambipolarity in the vicinity of edge islands, in a way that the potential has the same symmetry of the parent island [20].

New RFX measurements show that the plasma kinetic response is far from being a simple $1/7$ helix [21, 22]: due to toroidicity, an m/n mode always generates $(m \pm k)/n$ higher harmonics, $k = 1, 2, \dots$, with the same n . In this paper we will show the effect of these higher $m \pm k$ modes on the edge magnetic topology of RFX-mod: in particular, we will concentrate our attention on the $k = 1$ sideband, which is by far the dominant one, and in particular on the $0/7$ mode, which is the one resonating in the edge. We will show that, by measuring kinetic quantities in a particular θ, ϕ location, one can incur in substantial errors or mis-interpretations of the kinetic plasma response: only a full 3D coverage of θ, ϕ angles can reveal the real topology of the plasma. This can be a caveat for MP application in tokamaks, because it shows that toroidal and poloidal sidebands, though smaller than the base mode by a factor $\sim \epsilon = a/R$ [23], can have a sizable effect on the kinetic response of the edge plasma, and thus on ELM-related issues.

2. Mode spectra and basic properties of the RFP helical topology

The RFP is characterized by a saturated spectrum of stationary tearing modes (TM), with main helicities $m = 0, 1$ and $0 < n \lesssim 20$ [24], whose amplitude and phases are measured in great detail. At high ($I_p > 1$ MA) current, the RFP shows a typical high-confinement helical state, dubbed quasisingle

helicity—QSH, where the entire plasma column is moulded as an helix (see [25] and references therein). Very pure QSH states have been obtained in the Reversed Field eXperiment—modified (RFX-mod) in Padua, Italy [26], where a state-of-the-art feedback control system of the tearing modes [27] allows for obtaining an *almost monochromatic* TM spectrum, with a strong, dominant $q = m/n = 1/7$ mode resonating in the plasma core [28].

Our case study is a typical QSH discharge, #37537 at $t = 130$ ms, with plasma current $I_p = 1.5$ MA and on-axis magnetic field $B = 1.4$ T. Eigenfunctions for the TMs are calculated with the NCT code, by solving the Newcomb’s equations in toroidal equilibrium, using as constraints the pick-up coil measurements in the edge [23]. The eigenfunction profiles are then inserted in ORBIT, which is a Hamiltonian guiding-center code in Boozer coordinates, (ψ_p, θ, ζ) [7]. Eigenfunctions are treated in the general representation $\delta \vec{B}_{m,n} = \nabla \times (\alpha_{m,n}(\psi_p) \vec{B}_0)$, with \vec{B}_0 the equilibrium field [29, 30]. The application to the RFP tearing modes introduces spurious components in the longitudinal direction, whose contribution to topology and transport is absolutely negligible [31]. The spectrum of TM is shown in figures 1: figure 1(a) shows the $m = 1$ component, while figure 1(b) shows the $m = 0$ component of the spectrum. In figure 1(a) it is evident the presence of the $1/7$ mode, one order of magnitude larger than the other $n > 7$ modes. The $1/7$ mode is the innermost resonant TM, given the value of the safety factor on axis, $q(0) \sim 0.15$, which is typical of RFX-mod [32]. The $m = 0$ spectrum shows a similar, almost monochromatic shape (figure 1(b)). It is worth noting that the large $0/7$ mode appears only in the Newcomb analysis in toroidal geometry (red lines in figure 1(b)), while in cylindrical geometry (lines in cyan) the spectrum is flatter (with peaks at $n = 8, 13$ and 19). In fact, the $0/7$ mode is generated by the $1/7$ via toroidal coupling, the $\pm 1/0$ mode being the ‘mediator’ between modes with the same toroidal number [23]. This interaction is a geometrical effect of the Shafranov shift: as such, the $0/7$ mode inherits the same rotation frequency and a well-definite phase relation with the parent $1/7$ mode.

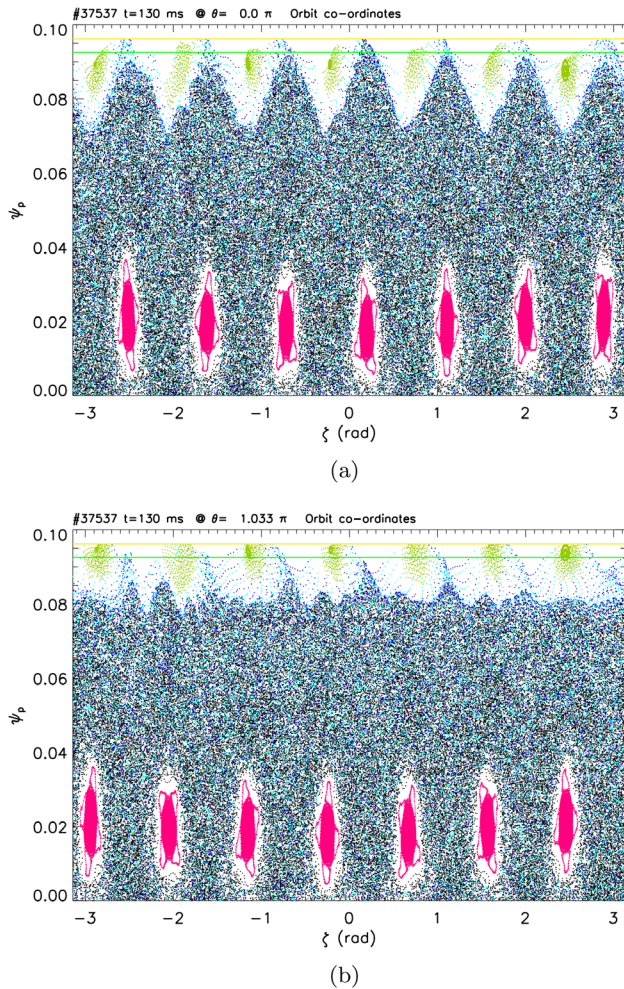


Figure 2. Poincaré plot of RFX-mod helical topology, equatorial cut at (a) $\theta = 0$ and (b) $\theta = \pi$. The green, horizontal line is the reversal surface at $q = 0$, the yellow one is the wall.

The Poincaré map of the helical state of RFX is shown in figure 2: generally speaking, it shows a marked similarity with the tokamak edge, when RMPs are applied (see e.g. figure 3 in [33]), provided the toroidal angle in the RFP is substituted for the tokamak poloidal angle. The $1/7$ mode determines a large, conserved structure in the core (pink points), corresponding to the strong core temperature increase observed in the QSH state [25]. Conserved islands (light green points) are seen also in the RFX edge, near the reversal surface at $q = 0$, which is marked as an horizontal, green line in figure 2: those are the $0/7$ islands, which correspond to the resonant response to the toroidally coupled $m = 0$ mode. At mid-radius, the overlap between $n > 7$ resonances determines a chaotic sea, which extends to the X-points (XP from now onward) of the $0/7$ islands. The $1/7$ mode is so strong that determines a $n = 7$ wiggle in the chaotic sea, up to the edge (the modulation of black points near the reversal in figure 2, sometimes referred to as *magnetic flutter* [34]). This magnetic-flutter can be analytically determined from the original Hamiltonian of field lines through a canonical transformation [35]. It is the competition between the $m = 0$ islands in the edge, and the $1/7$ magnetic flutter, that determines the plasma-wall interaction, as already anticipated in the past on RFX [36]. In particular, this

competition depends on the phase relation between the $1/7$ and the $0/7$ modes. In RFX, it is observed that these modes have typically the same phase at $\theta = \pi$ [23]: topologically, this translates in the O-points (OP) being aligned along the toroidal angle ζ , in the Poincaré section at $\theta = \pi$, as shown in figure 2(b). Consequently, at $\theta = \pi$ the magnetic flutter limits the size of $0/7$ islands towards the edge, as we will consider in more detail later in section 3. Conversely, at $\theta = 0$ the OP's of the $1/7$ correspond to the XP's of the $0/7$, since the $m = 0$ structure does not change by varying the surface of section, while the $m = 1$ structure advances of $\pi/7$ in the positive ζ direction, when θ is increased (see figure 2(a)). In this case, the magnetic flutter moves radially outwards, into the weakly chaotic region of the $0/7$ XP's, and touches the wall. This aspect will also be expanded in section 3.

Despite this tangled topology, in the past a very good agreement has been found between a simple, helical $1/7$ symmetry and measurements of floating potential, edge electron pressure and $\vec{E} \times \vec{B}$ flow [8–15]. Nevertheless, those measurements were performed along the toroidal angle ϕ , at two fixed poloidal locations $\theta = 0, \pi$ (the same as in figure 2). Little or no information was available along the poloidal direction. As we will see in the following sections, this lack of poloidal information led to the erroneous belief that edge kinetic quantities F_k followed a *perfect helical shape*. Accordingly, a helical angle was introduced as

$$u(\theta, \phi; t) = m\theta - n\phi + \omega_{m,n}t. \quad (1)$$

The initial phase of the mode was chosen in a way that $u_{1,7} = \pi/2$ corresponds to the OP of the $1/7$ island, while $u_{1,7} = 3\pi/2$ corresponds to the XP [10]. The helical angle provides a unique way of mapping diagnostics placed at different θ, ϕ to the helical topology, and the conclusion was that all kinetic quantities followed the helix, or that $F_k \approx \sin u_{1,7}(\theta, \phi; t)$ ('harmonic' approximation).

A hint that kinetic quantities could follow a shape more complicated than u , with an additional dependence on θ , was anyway shown in [10]: in particular, figure 8 in that paper shows a possible role of the $0/7$ islands, and figure 8(c) in [8] shows that the floating potential V_f jumps from $\theta = 100^\circ$ to 250° with no smooth dependence on time, during a single $1/7$ island rotation period.

New measurements of electron pressure in RFX, performed with two twin thermal helium beam (THB) diagnostics placed at $\theta = 0, 90^\circ$ and the same toroidal angle [37], clearly show that the harmonic approximation does not hold. In figure 3 the time traces of the two THB monitors are shown: the signals are perfectly in-phase. If they followed the helical angle, equation (1) with $m = 1$, the two signals should be out of phase by an amount $\Delta t = -\pi/2\omega$, but this is clearly not the case. To solve this conundrum, we should analyze more in detail the topology of the RFX edge.

3. Edge structures: islands and stochastic layers

Given the spectrum of the helical RFX edge, figure 1, it is useful to analyze a simplified Poincaré plot where we insert as input the $n = 7$ modes, only. This should highlight the

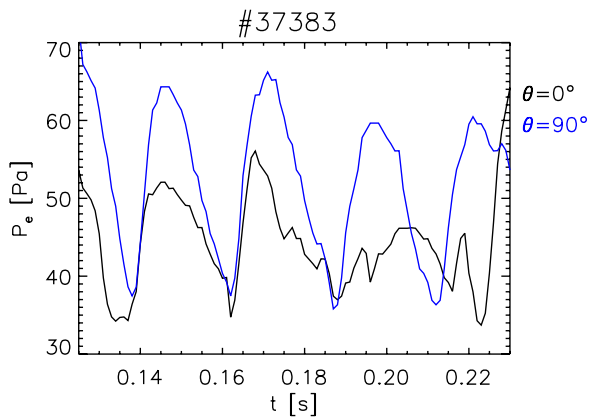


Figure 3. Time traces of electron pressure P_e , measured with two thermal helium beam diagnostics placed at $\theta = 0, 90^\circ$ in the same toroidal section on RFX-mod. The signals are clearly in-phase, apparently contradicting the harmonic approximation on the helical PWI.

fundamental features of the RFX topology. In fact, it is often the case that conserved structures are hidden in the complete Poincaré plots, such those of figure 2. Regarding the RFP, in the past this has been shown, for instance, in the case of bundles of field lines characterized by Lévy-flight statistics, embedded in the chaotic sea (see figure 2 in [38]). More recently, hidden structures have been detected in the vicinity of the large, core islands (the pink ones in figure 2), as local maxima in the 3D map of finite-size Lyapunov exponents [39].

3.1. Stochastic layers

In our case study, the simplified Poincaré with $n = 7$ modes only, is shown in figure 4. The plot shows immediately that the dominant structures in the edge are:

- the $0/7$ islands, which determine the last closed-flux surface (LCFS), which is the cyan, solid curve near the edge. In the plot, the LCFS is calculated as the envelope of the last intersections of the field lines [22], before hitting the wall (horizontal yellow line);
- the stochastic layer, which is the blue band of points separating the volume of field lines orbiting around the $0/7$ islands in the edge, from the volume of field lines orbiting around the $1/7$ islands in the core [40]. It is worth noting that the stochastic layer is a more rigorous definition of the magnetic-flutter shown in figure 2.

In the Poincaré plot at $\theta = 0$, figure 4(a), it is evident that the outermost structure touching the horizontal yellow line representing the wall, is the stochastic layer: this is the consequence of the fact that the $1/7$ OP is aligned with the $0/7$ XP at $\theta = 0$, as anticipated in section 2. Besides this, in a toroidal system, O-points and X-points are not aligned radially along the rational surface (the $q = 0$ surface in our case). In fact, the solution to the tearing mode equation maps out *asymmetric islands* [41] with the OP shifted inwards and the XP outwards, with respect to $q = 0$. This is exactly the case of the $0/7$ islands in figure 4(a) (note that in RFX we solve the same equations used by Fitzpatrick in [41]).

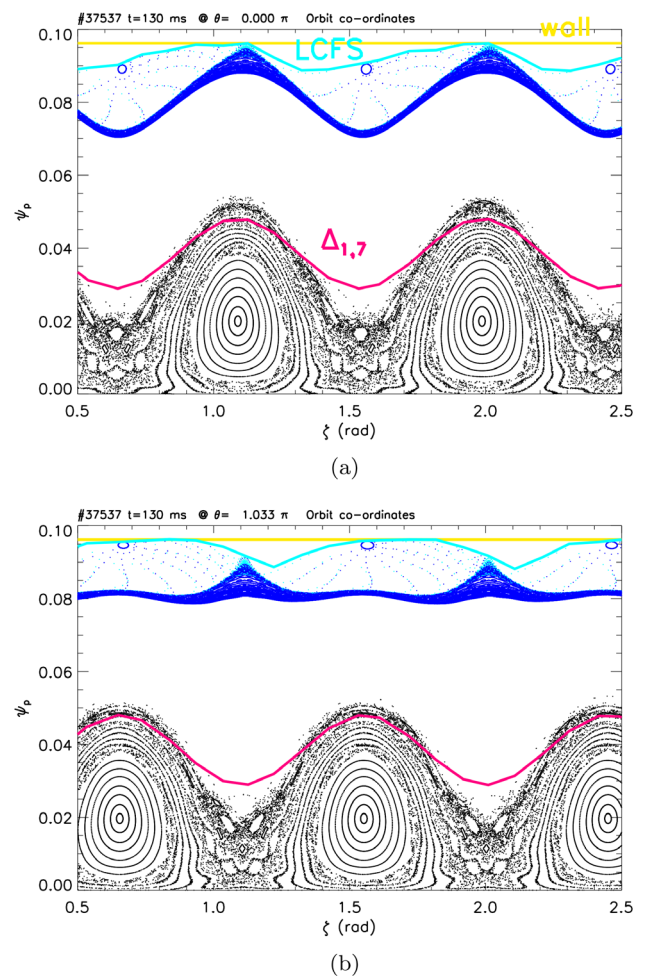


Figure 4. Poincaré plots of RFX-mod helical topology, equatorial cut at (a) $\theta = 0$ and (b) $\theta = \pi$. A simplified spectrum with $n = 7$ modes, only, has been used as input to ORBIT. The magenta curve near the $1/7$ islands corresponds to the ideal displacement of the $1/7$ mode (not to scale); the cyan, solid curve near the edge is the envelope of the last intersections of the field lines, before hitting the wall (horizontal yellow line). For the sake of simplicity, in this plot the unperturbed reversal is not shown.

Conversely, at $\theta = \pi$, figure 4(b), the stochastic layer is separated from the wall, and the outermost structure is the $0/7$ island (cyan, solid line). Since one can expect the stochastic layer to possess larger connection lengths (see section 4), this results in a modulation of the plasma-wall interaction (PWI) along both angles, θ and ζ . It is worth noting that the interplay between the stochastic layer and the $0/7$ island is intrinsically non-harmonic: to show this, in figure 4 the ideal displacement $\Delta_{1,7}$ of the dominant mode is plotted as a solid, pink line. By definition, it is $\Delta_{1,7} = \Delta(0) \sin u_{1,7}$ (see e.g. figure 1 in [10]). Therefore, if the harmonic approximation were satisfied, the LCFS should follow $\Delta_{1,7}$. While this is verified at $\theta = 0$ (figure 4(a)), at $\theta = \pi$ there is a shift of about ~ 0.3 radians in ζ , between $\Delta_{1,7}$ and the LCFS (figure 4(b)).

The mechanism of the interplay between stochastic layer and $0/7$ island in the edge, is made clear in figure 5. The radii of the $0/7$ islands O-points are plotted as a function of the poloidal angle. The $m = 0$ resonances are shifted inward or outward, depending on the relative phase of the $1/7$ and $0/7$

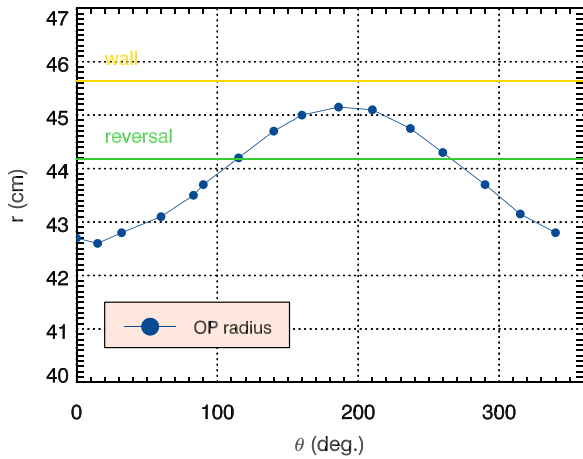


Figure 5. Radii of the O-points of the 0/7 islands, as a function of θ .

modes. Islands are closer to the wall at $\theta \sim 180^\circ$, the converse at $\theta = 0$: this is truly the $m = 1, n = 0$ toroidal effect described in [23]. Only at $\theta \approx 110^\circ, 260^\circ$ the $m = 0$ islands resonate at the unperturbed reversal surface (green line). This effect was already shown in figure 6 of [11]. Consequently, the 0/7 islands are responsible for the PWI at $\theta \sim 180^\circ$ (shorter connection lengths), while at $\theta = 0$ the stochastic layer dominates (longer connection lengths).

3.2. Edge islands

When the 0/7 island is the outermost structure touching the wall, as in figure 4(b), field lines are not uniformly distributed around the OP: in fact, the LCFS (cyan line in figure 4(b)) is not symmetric in ζ around the OP, but it is slanted to the right, in the direction of larger ζ . This is a common effect in classical mechanics: field lines circle around the island O-point with frequencies that depend on the distance from the O-point [42]. Figure 6 shows the time evolution of points placed initially at $\psi_p = 0.089, \theta = 0$ for a period of 9.14 ms (one toroidal transit of a field line on axis, $\tau_{\text{tor}} = 2\pi R/\nu_{\text{th}}$), with snapshots taken at fixed time intervals (0.55 ms, note that it is not a Poincaré plot!). The rotation rate (clockwise) clearly depends on the distance from the O-point, with faster rotation happening closer to it. Near the OP a full period is about 1.6 ms, while outer points do not finish one full period during the run time. In fact, the period around the OP is given by [43]:

$$T = \frac{1}{\sqrt{\bar{\alpha}}} K(\sin(Q_b/2)), \quad (2)$$

with $\bar{\alpha} = \alpha(r_s)$ amplitude of the TM at the resonance, where the profile $\alpha(r)$ is defined in section 2. K is the complete elliptic integral of first kind and $Q_b = u_{0,7} - \pi/2$. Practically speaking, this means that the period near the OP is $T \sim r_{\text{OP}}/\sqrt{\bar{\alpha}}$, which is proportional to the distance from the OP ('Kepler'-like law⁴). In this way, field lines tend to occupy

⁴This is a general law of Hamiltonian systems: a particular instance is the Keplerian system, for which the scalar function $\alpha(r)$ coincides with the gravitational potential $\alpha(r) \sim -1/r$. In that case $T \sim r/\sqrt{\bar{\alpha}} = r^{3/2}$, which is Kepler's third law.

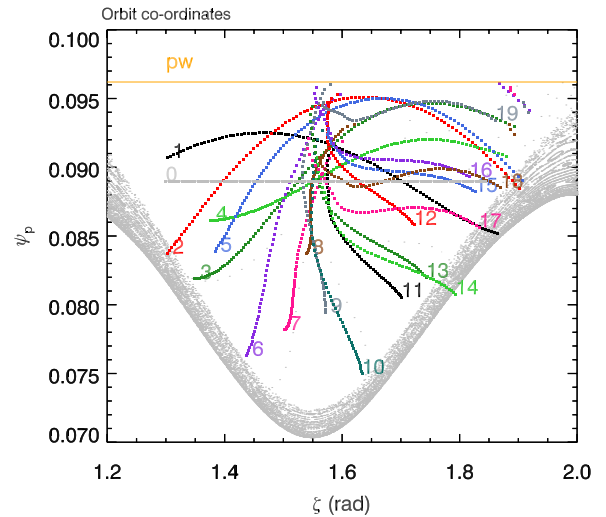


Figure 6. Snapshots of field lines taken at fixed time intervals (0.55 ms), for a period of 9.14 ms (one toroidal transit), showing the variation of the rotation rate as a function of increasing distance from the OP. Points are initially placed at $\psi_p = 0.089, \theta = 0$. Over-plotted is the Poincaré plot of the stochastic layer, to give a reference with the topology shown so far.

the region to the right of the OP, which is the effect of orbits lagging behind in the clockwise rotation around the OP. One can then expect a shorter connection length to the right of the OP, since the region to the left is devoid of field lines.

4. Connection lengths

In sections 2 and 3, we have provided a qualitative description of the edge topology in the helical RFX: now it is necessary to give a quantitative description. As a statistical indicator of the interaction between the topology and kinetic properties of the edge plasma, we can use the connection length to the wall, $L_{c,w}$. Introduced in TORE SUPRA to describe the number of toroidal turns that magnetic field lines run to connect the modules of the ergodic divertor to the wall [44], it has since then been extensively used in RMP literature: some examples include DIII-D [16], TEXTOR [3, 33], MAST [45] and ASDEX Upgrade [6]. The rationale is that electrons follow closely the field lines, so that regions of low $L_{c,w}$ are regions of increased parallel electron losses. The results presented in this section should clarify the effect of the 0/7 sideband in determining electron transport in a stochastic layer produced by MPs, which is of critical importance for tokamaks.

We apply the calculation to the case of figure 2, using the full $m = 0, 1$ and $n \leq 24$ spectrum of TM. Initial and final conditions are $(\psi_{p,0}, \theta_0, \zeta_0)$ and $(\psi_{p,w}, \text{random}, \text{random})$, where $\psi_{p,w}$ is the poloidal flux at the wall. The initial conditions are then varied (for each run) on a grid $(\psi_{p,j}, \theta_k, \zeta_l)$, with $1 \leq j \leq 7$, $1 \leq k \leq 16$, $1 \leq l \leq 64$, and boundaries $0.090 \leq \psi_p \leq 0.096$ and $-\pi \leq \theta, \zeta \leq \pi$ (the radial boundary corresponds in real space to $40.8 \leq r \leq 45.6$ cm, being the minor radius $a = 45.9$ cm and the unperturbed reversal $r_{\text{rev}} = 44.2$ cm). Each run comprises 1000 collisionless, low energy (10^{-5} keV) ions, which mimic a field line [31], all initiated at the same $(\psi_{p,j}, \theta_k, \zeta_l)$ on the grid of initial conditions. The connection

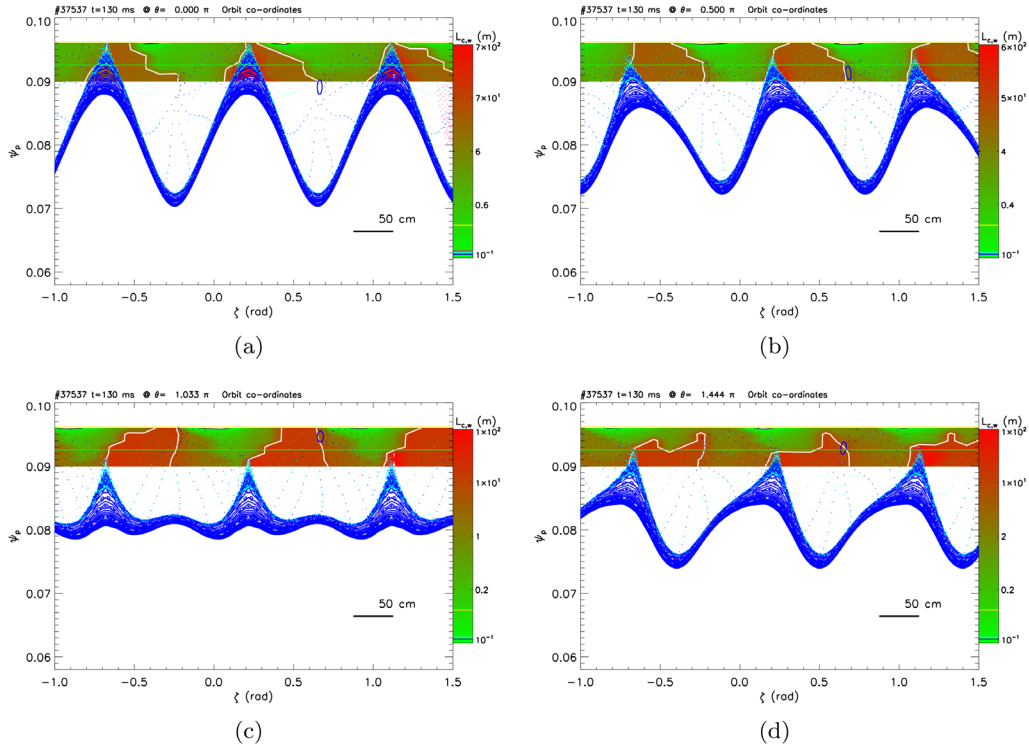


Figure 7. Contour plots of connection length $L_{c,w}$ on the equatorial plane (ζ, ψ_p), at four poloidal angles, $\theta = 0, 90^\circ, 186^\circ$ and 260° . Overplotted, the Poincaré plots of the helical topology, simplified spectrum with $n = 7$ modes, only. The unperturbed reversal is the horizontal, green line, the wall is the yellow line. The white contour corresponds to the Kolmogorov length L_k , and separates laminar and ergodic regions.

length is then defined as $L_{c,w} = \langle L \rangle$, i.e. the average over the particles of the parallel length travelled along the field line, until they are lost on the wall, $L = v_{th}\tau_{loss}$. This definition of $L_{c,w}$ is the same as that used with ORBIT in a recent work on TEXTOR [46], and matches the definition which is found in tokamak literature [3, 16, 33, 45]. A first definition, with a fixed initial condition and variable final points, was used in previous works on RFX [10, 12], but in the present study was rejected and modified in favor of the more standard usage, since it does not reproduce details of pressure and floating potential measurements for shot #37537 and similar ones. This is a caveat for the use of $L_{c,w}$, since it shows that this statistical indicator is ill-defined: in particular, it depends on the choice of the initial and final conditions. We will come back again on this issue in section 5. Finally, to distinguish between laminar and ergodic regions, we estimated the Kolmogorov length L_k through the procedure of the finite-size Lyapunov exponents (FSLE), described in [31]. We deposited 7000 field lines at $\psi_p = 0.07$, and the result is $L_k = 10.8$ m (0.86 toroidal turns). This is only a reference value, and a more precise, local calculation will be given via a different method in section 5.

Given the intrinsic 3D nature of the problem, it is necessary to plot $L_{c,w}$ in all three directions, (ψ_p, θ, ζ) : figure 7 shows the contour plots of connection length $L_{c,w}$ on the equatorial plane (ζ, ψ_p), at four poloidal angles, $\theta = 0, 90^\circ, 186^\circ$ and 260° . In the four panels, the white contour level corresponds to $L_{c,w} = L_k$, and separates laminar ($L_{c,w} < L_k$) from ergodic regions ($L_{c,w} > L_k$). In the tokamak community, this is a standard way of highlighting regions of strong interaction,

i.e. those with $L_{c,w} > L_k$ [47]. In figure 7, all of the main features discussed in section 3 can be recognized: in particular, $L_{c,w}$ is a factor ~ 6 longer at $\theta = 0, 90^\circ$, and it is shorter at $\theta = 186, 260^\circ$. Moreover, two very distinct behaviors can be recognized:

- (i) At $\theta = 0, 90^\circ$ the PWI is dominated by the stochastic layer (section 3.1), which is closer to the wall and is characterized by $L_{c,w} > L_k$ (red regions). In particular, moving from $\theta = 0$ to $\theta = 90^\circ$ does not change the position of the maximum $L_{c,w}$ along ζ , which sticks to the toroidal location of the XP of the 0/7 island. This justifies the fact that signals of electron pressure and floating potential are *in phase* at $\theta = 0, 90^\circ$ (same toroidal section), as shown in figure 3;
- (ii) at $\theta = 186, 260^\circ$ the PWI is completely dominated by the 0/7 islands, following what shown in figure 5. The ‘Kepler’-like motion of field lines around the OP of the 0/7 island (figure 6) determines the formation of laminar pockets to the right of the OP, as described in section 3.2. Conversely, to the left of the OP an ergodic region forms, with $L_{c,w} > L_k$: it is this region now, that dominates PWI. Again, moving from $\theta = 186^\circ$ to $\theta = 260^\circ$ does not change the position of the maximum $L_{c,w}$, which is now close to the OP of the 0/7 island. Again, signals of floating potential are *in phase* at 186, 260°.

Summarizing, more than a helical shape, the PWI seems to be the combination of two regions of $m = 0$ interaction, $0 < \theta < 90^\circ$ and $180 < \theta < 260^\circ$, arranged along a helix.

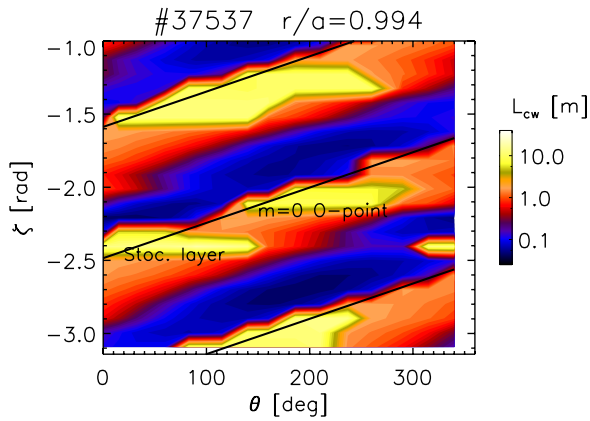


Figure 8. Contour plot of $L_{c,w}$ @ $\psi_p = 0.096$ (the last point in the radial mesh), on the (θ, ζ) plane. The continuous, black lines mark the location of the OP of the $1/7$ island: they correspond to $u_{1,7} = \pi/2$, or $\zeta = \theta/7 - \pi/14 - 2k\pi/7$, $k \in \mathbb{Z}$. It is clear that the PWI has a strong, non-helical component due to the $m = 0$ mode.

Therefore, *PWI is dominated by the toroidal sideband of the base mode*, which is a strikingly new result with respect to previous RFP and tokamak literature. This is made evident if one plots the contour of $L_{c,w}(\psi_p, \theta, \zeta)$ at the outermost point of the radial grid, $\psi_p = 0.096$, on the (θ, ζ) plane. This is shown in figure 8: the contour is characterized by two horizontal stripes of large $L_{c,w}$ at constant ζ , the first generated by the stochastic layer and the second by the $0/7$ islands, respectively. Actually, this was shown already in a previous paper (figure 9 in [36]), but the authors in that paper neglected the role of poloidal sidebands. The deviation of the real PWI from a helix is highlighted in figure 8 by plotting the location of the OP of the $1/7$ helix as a continuous, slanted line.

Another way of showing the deviation of the PWI pattern from a helix is by calculating the maximum of $L_{c,w}(0.096, \theta, \zeta)$ along ζ , say ζ_{\max} , for each value of θ in the poloidal grid. One can then translate the values (ζ_{\max}, θ) in helical angles using equation (1), and considering the variation of $u_{1,7}^{\max}$ along θ . As anticipated in section 2, if the PWI followed a perfect helical shape, $u_{1,7}^{\max}$ should be constant along θ : for example, it should be $u_{1,7}^{\max} = \pi/2$ if it followed the $1/7$ OP [10]. In figure 9 the maximum $u_{1,7}^{\max}$ is plotted in orange, the light-orange shaded region highlighting the width at half maximum (FWHM) of $L_{c,w}$. The shape and the position of the maximum depend on the poloidal angle θ , contrary to the helical ('harmonic') approximation: at $\theta = 0$, the maximum of the connection length is at $u_{1,7} \approx \pi/2$, with a narrow distribution; then moving towards $\theta \sim 140^\circ$, the maximum moves up to $u_{1,7} \sim \pi$, and the distribution becomes wider; then it moves back to $\pi/2$ at $\theta = 180^\circ$. The change in the shape of $L_{c,w}$ is due to the different pattern of the stochastic layer, with a narrow, 'V'-shaped topology (see figure 7(a)), if compared to the broader $0/7$ islands (see figure 7(c)). The dependence of $u_{1,7}^{\max}$ on θ is another way of stating that there are regions of the plasma where the dependence is not $m = 1$, but $m = 0$. Besides this, figure 9 also shows that, if one considers *only two* probes placed at $\theta = 0, 180^\circ$, the maximum $u_{1,7}^{\max} \approx \pi/2$, i.e. it reproduces a perfect helical shape. This was reported in the past on RFX, based on measurements performed on the equatorial plane, only [8–15]. The

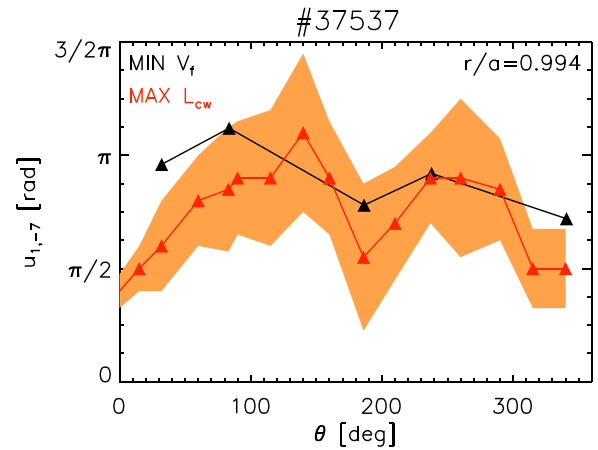


Figure 9. Location of maximum $L_{c,w}$ @ $\psi_p = 0.096$ and minimum floating potential V_f in the helical angle $u_{1,7}$, as a function of the poloidal angle θ . This plot shows the deviation of $L_{c,w}$ and V_f from the helical shape. The colored band around $L_{c,w}$ is the FWHM.

new pattern of $L_{c,w}$ reproduces quite well experimental data: in figure 9 black triangles are the position (in $u_{1,7}$) of the minimum of the floating potential V_f , measured with a poloidal array of 5 internal probes belonging to the ISIS system [48], and averaged over ~ 20 discharges. There is a caveat while comparing $L_{c,w}$ and V_f , since the first is the result of ORBIT simulations at a fixed time instant, while V_f is a measurement averaged over many times and shots. Despite this, the agreement is quite good, showing that V_f , too, does not follow a straight, horizontal line. The deviation of $L_{c,w}$ and V_f from a helix is of the order $\Delta u_{1,7} \sim 90^\circ$, which is $\sim 25\%$, approximately a factor $\sim \epsilon = a/R$, consistent with the magnitude of the toroidal effects on RFX [23]. Similar effects are to be expected in the tokamak edge, when MPs are applied: but to reveal them, a thorough 3D analysis of magnetic inputs and kinetic outputs should be undertaken.

5. Definition and use of the Poincaré recurrence time

As explained in section 4, in presence of tangled topologies, such as those of the RFX edge and tokamak stochastic layers, the connection length $L_{c,w}$ becomes ill-defined: in particular, it depends on the choice of the initial and final conditions. To assess the role of sidebands in determining the plasma response to a base mode, it is therefore necessary to introduce a probabilistic description of chaos, namely the *Poincaré recurrence time*. This is a unequivocally defined property of a bounded area A . In fact, the Poincaré theorem of recurrences states that for any initial condition in A , trajectories will repeatedly return to A if the dynamics is area-preserving, such is the case of the magnetic field for which $\nabla \cdot \vec{B} = 0$. The theorem has a general applicability, since it is valid for all systems satisfying the Liouville theorem on the preservation of phase volume [49]. The statistics of the recurrence times reflect any non-uniformity in the phase-space, and they are used in Hamiltonian chaos theory to map systems with a stochastic sea and islands: the topology of the RFX edge

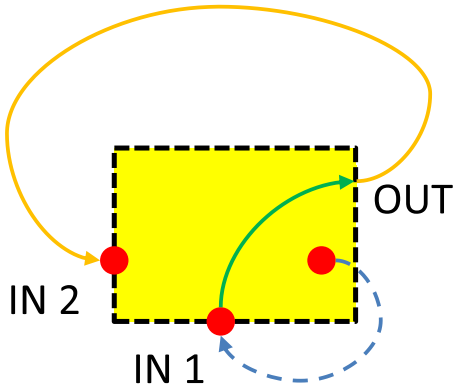


Figure 10. Sketch for the definition of the Poincaré recurrence time: the domain A is the yellow rectangle, the ‘escape’ time corresponds to the green solid trajectory, while the ‘external’ time corresponds to the orange solid trajectory. The first trajectory out of A is the dashed line, and it is neglected in the calculation.

(and that of tokamaks with MPs) is therefore an ideal case to exploit this method. Even though the concept of recurrences is not new in plasma physics (an instance is the application of *recurrence plots* [50] to time-series analysis of electrostatic turbulence [51]), this is the first time that a rigorous definition of Poincaré recurrence is applied to a fusion device.

Following Zaslavsky [49], we define a bounded area A of volume $\Gamma(A)$, sketched in figure 10 as a yellow rectangle. We can define an *escape time* from A as the time spent inside the volume A , i.e. the interval between the first entrance t_{IN1} and the (second) exit time t_{OUT} :

$$\tau^{(esc)} = t_{OUT} - t_{IN1}. \quad (3)$$

The escape time is shown as a green solid line inside area A in figure 10. The first trajectory, from the deposition point to the first entrance t_{IN1} , is shown as a dashed line in the same figure, and it is neglected since the first time a particle exits A it lacks a correct definition of the escape time. Similarly, we introduce the time a particle spends outside A , as the time between the exit time t_{OUT} and the second entrance t_{IN2} :

$$\tau^{(ext)} = t_{IN2} - t_{OUT}. \quad (4)$$

This ‘external’ time is shown as an orange solid line in figure 10. The *recurrence time* is the time spent out plus the escape time, and thus:

$$\tau^{(rec)} = \tau^{(esc)} + \tau^{(ext)} = t_{IN2} - t_{IN1}. \quad (5)$$

Therefore, to map the recurrence times in A , it is necessary to record only two successive entrance times, for each particle: the exit times do not carry relevant information. Mathematically speaking, the recurrence time is defined as the limit $\lim_{\Gamma(A) \rightarrow 0} \tau^{(rec)}$ [49], so the volume $\Gamma(A)$ should be small with respect to the system size. In this way, the Poincaré recurrence time becomes truly dependent on the volume area A only, thus being a better observable than the connection length $L_{c,w}$.

The area A to determine the Poincaré recurrences is easiest defined as a closed ellipsoid centered in $(\psi_{p,0}, \theta_0, \zeta_0)$, and bounded by the surface defined according to:

$$R_e^2 = 2\pi \left(\frac{\psi_p - \psi_{p,0}}{\psi_{p,w}} \right)^2 + (\sin \theta - \sin \theta_0)^2 + (\cos \theta - \cos \theta_0)^2 + (\sin \zeta - \sin \zeta_0)^2 + (\cos \zeta - \cos \zeta_0)^2. \quad (6)$$

The ‘radius’ R_e of the ellipsoid is chosen as to be comparable to the grid spacing of section 4; the 2π factor in front of the first term in the r.h.s. of equation (6) is necessary for reducing the elongation of the ellipsoid in the radial direction.

While the existence of the recurrence time is guaranteed by the theorem proved for the first time by Poincaré, the practical applicability of this observable relies on the estimate of the average τ_{rec} over a distribution $P(t)$. In fact, one can define a probability distribution function (p.d.f.) of recurrences t , with $P(t)dt$ the probability for $\tau^{(rec)}$ of falling between t and $t + dt$. Then the *mean* recurrence time τ_{rec} can be introduced as [49]

$$\tau_{rec} = \frac{\int_0^{+\infty} t P(t) dt}{\int_0^{+\infty} P(t) dt}. \quad (7)$$

Boltzmann, in a reply to Ernst Zermelo, was the first to show that, in a perfect gas, the Poincaré recurrence time calculated according to equation (7) is overwhelmingly large [52]. A more general estimate is given by the Kac lemma [49] as

$$\tau_{rec} = \Delta t \frac{\Gamma}{\Gamma(A)} < \infty, \quad (8)$$

where Δt is the time between two successive interceptions in the Poincaré plot, Γ the total volume of the phase space. In the case of a toroidal RFP, figure 11 shows an example of calculation of $P(t)$ in a sample volume near the 0/7 island XP, just within the stochastic layer described in section 3. The equatorial section of the volume defined according to equation (6) is shown in figure 11(a) as a pink, shaded area. In this case, the Kac formula (8) can be simplified to

$$\tau_{rec} \approx \tau_{tor} \frac{2\pi^2 a^2 R}{\Gamma(A)} = \frac{3}{2} \pi \tau_{tor} \left(\frac{a}{\Delta r} \right) \frac{1}{\Delta \theta \Delta \zeta} = 290 \tau_{tor}, \quad (9)$$

where $\Gamma(A) = 4/3 \pi \Delta r (a \Delta \theta) (R \Delta \zeta)$ is the volume of the ellipsoid defined in equation (6). Therefore, in the RFP, contrary to the famed Boltzmann case, the average recurrence time is well within computational capabilities.

For each particle we record successive recurrence times (equation 5), restarting each particle that has returned the volume with random position inside A . The p.d.f. of recurrences is shown in figure 11(b). It can be demonstrated [49] that in a homogeneous, uniform, fully chaotic system with a Chirikov parameter well above the stochastic threshold [53], the p.d.f. of recurrences follows the exponential law:

$$P(t) = \frac{1}{\tau_{mix}} \exp \left(\frac{-t}{\tau_{mix}} \right), \quad (10)$$

and that $\tau_{mix} v_{th} = L_k$, with L_k the Kolmogorov length. Trajectories for which scaling (10) applies are called ‘uniform mixing’ [49] because of the absence in phase space of singular zone domains with zero Lyapunov exponents (or infinite L_k , conserved domains), such as the pink and green islands of figure 2. We will therefore call the correspondent

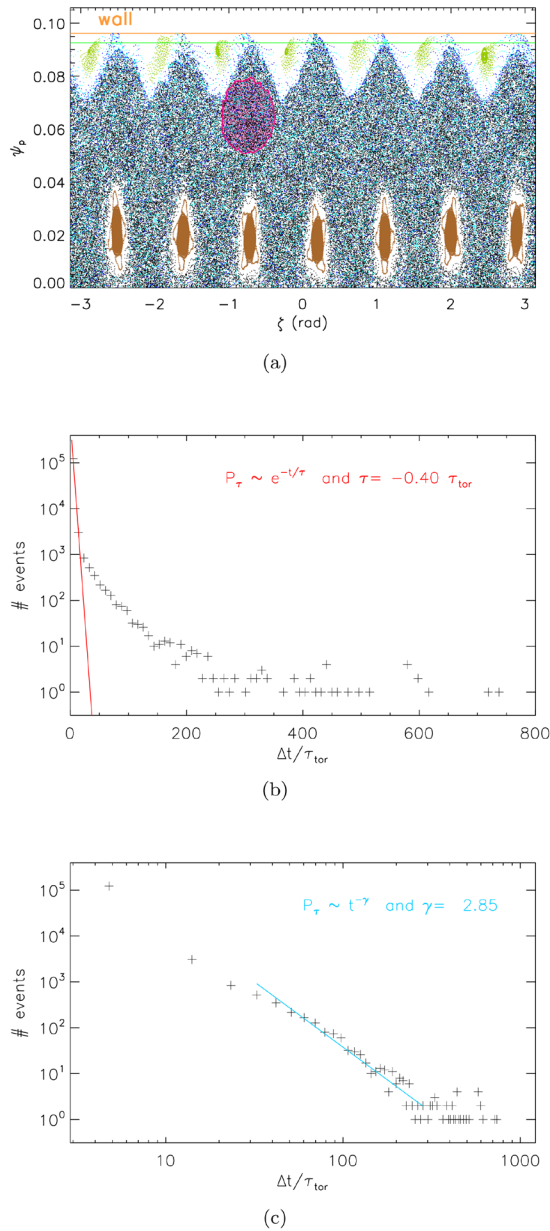


Figure 11. Poincaré recurrence time in a chaotic domain (a) Poincaré plot at $\theta = 0$, the pink shaded area is the area A to calculate recurrences; (b) p.d.f. of recurrences, logarithmic plot: the red line shows the initial exponential decay; (c) p.d.f. of recurrences, bi-logarithmic plot, to show the power law of the tail.

exponent the ‘mixing’ recurrence time, τ_{mix} . Figure 11(b) shows anyway that, in the stochastic edge of the RFX (and, by similarity, in the ergodic edge of a tokamak with RMP) a long tail of sub-exponential, or power law, appears. This tail is evident in figure 11(b), and it is formed by points placed *to the right* of the red line interpolating the initial, exponential decay $P(t) \sim e^{-t/\tau_{\text{mix}}}$. This means that there is a non-negligible fraction of particles with $t \gg \tau_{\text{mix}}$, that are trapped in islands and ‘sticky’ regions with nearly zero Lyapunov exponents, such as islands and the stochastic layer of figure 4, before re-entering area A. As a consequence, the average recurrence time defined in equation (7) is larger than the ‘mixing’ time, $\tau_{\text{rec}} > \tau_{\text{mix}}$. In figure 11(b) the exponential

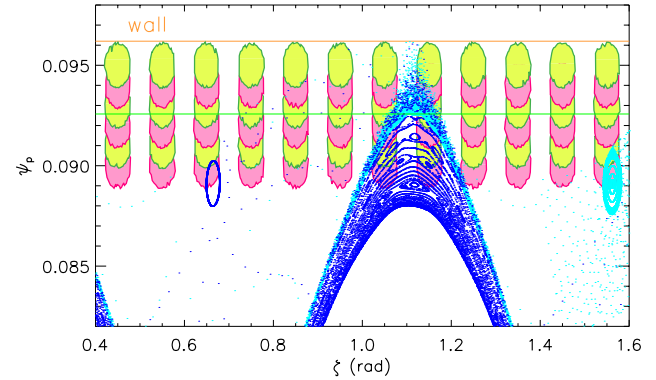


Figure 12. Definition of the volumes to calculate Poincaré recurrences: the volumes are arranged in a 12×6 array in the (ζ, ψ_p) plane at $\theta = 0$.

time is $\tau_{\text{mix}} = 0.4\tau_{\text{tor}}$, corresponding to $L_{\text{mix}} = 5$ m, while the (average) recurrence time is $\tau_{\text{rec}} = 6\tau_{\text{tor}}$, corresponding to $L_{\text{rec}} = 76$ m. These values are compatible both with $L_k = 10.8$ m estimated in section 4, and with the value of $L_{c,w}$ of figure 7(a). The tail is shown in the bi-logarithmic plot of figure 11(c) as a blue, solid line, and shows that for $t > t^* \sim 30\tau_{\text{tor}}$ the p.d.f. of recurrences follows the power law

$$P(t) \sim t^{-\gamma}, \quad (11)$$

with $\gamma = 2.85$. This value of the exponent is compatible with the value $\gamma = 3$ that in chaos theory is found for the Sinai billiard [54]. Moreover, according to the Kac lemma (8) applied to an algebraic tail, any value $\gamma > 2$ is an unambiguous proof of the existence of ‘dynamical traps’ in the system, such as islands and sticky regions with zero Lyapunov exponents.

It is worth noting that the presence of a sizable, power-law tail in the recurrences p.d.f. $P(t)$ is consistent with the sub-diffusive nature of transport, which was already pointed out in chaos studies of the RFP [38, 55, 56]. This confirms also that chaos in fusion plasmas is too close to the stochastic threshold, to apply the random phase approximation. In other words, it is far from being homogeneous and uniform, so that the Rechester-Rosenbluth formalism [57], and the related quasilinear diffusive scheme, though quite popular in the field, is an overly crude simplification of the system dynamics (for a review of these issues, see [58]).

Now, let us use Poincaré recurrences to characterize the stochastic edge of RFX-mod. We start from the case shown in figure 7(a), and we restrain our analysis to a single $n = 7$ period along the toroidal angle. Define an array of 12×6 volumes in the (ζ, ψ_p) plane at $\theta = 0$, calculated according to equation (6): the array is shown in figure 12. For each volume we calculate a p.d.f. of recurrences, and a mean recurrence time τ_{rec} through equation (7). For the sake of comparison with the connection lengths, we determine the recurrence length $L_{\text{rec}} = \tau_{\text{rec}} v_{\text{th}}$. The comparison between $L_{c,w}$ and L_{rec} is shown in figure 13: the first noteworthy feature arising from figure 13(b) is that L_{rec} is not defined in a large part of the edge domain, namely in the laminar regions with $L_{c,w} < L_K$. This comes naturally from the fact that $\tau_{\text{rec}} > \tau_{\text{mix}}$ practically by definition (figure 11(b) and equation (10)), and that $L_k = \tau_{\text{mix}} v_{\text{th}}$: in the laminar regions, particles (field lines) are lost before

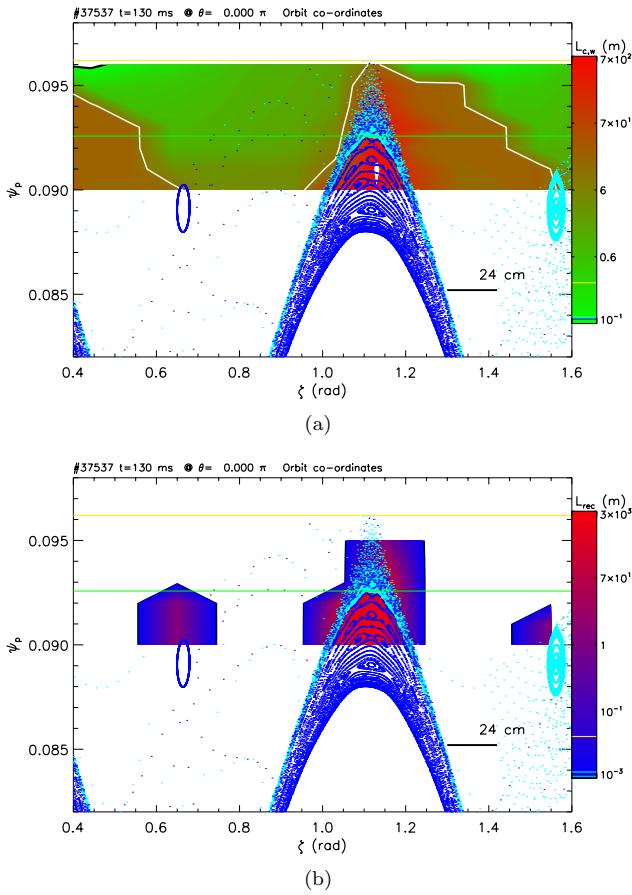


Figure 13. Comparison of two different chaos metrics, the connection length $L_{c,w}$ and the Poincaré recurrence ‘length’ $L_{rec} = \tau_{rec} v_{th}$, τ_{rec} being the Poincaré recurrence time: (a) is a zoom of figure 7(a) along a single $n = 7$ period in the toroidal angle ζ ; (b) is a contour of L_{rec} in the same region. The poloidal section is at $\theta = 0$.

they can return at least once to area A. On the contrary, the two main features determining transport in the edge emerge quite well: they are the stochastic layer ($L_{rec} \sim 1.5 \div 2$ km) and the edge $m = 0$ islands ($L_{rec} \sim 3 \div 4$ m: for the sake of comparison, 1 toroidal turn = 12 m in RFX, so 100 toroidal turns = 1.2 km). Therefore, at $\theta = 0$ the structure closer to the wall is the stochastic layer, with large Poincaré recurrence times (>100 toroidal turns). This confirms, on grounds of a mathematically better defined metric, the fact that particles inside the ‘ergodic’ region [3, 33] experience many times the whole plasma volume, before returning to their starting point: this is consistent with a larger temperature inside the ergodic region, both in tokamaks [4] and in RFX-mod [21]. Particles around the OP of the edge islands experience only partly the plasma volume ($\tau_{rec} \sim 1$ toroidal turn), and particles in the laminar regions experience none, they are rapidly lost to the wall. In this respect, from the point of view of recurrences, regions with $L_{c,w}$ in the range $1 - 100$ m are indistinguishable, no particle returns to area A (see the correspondence between the white regions in figure 13(b) and the contour levels in figure 13(a)). Therefore, discussing tiny variations of $L_{c,w}$ in the meter-to-kilometer range might not add significant information, even in the tokamak MP case.

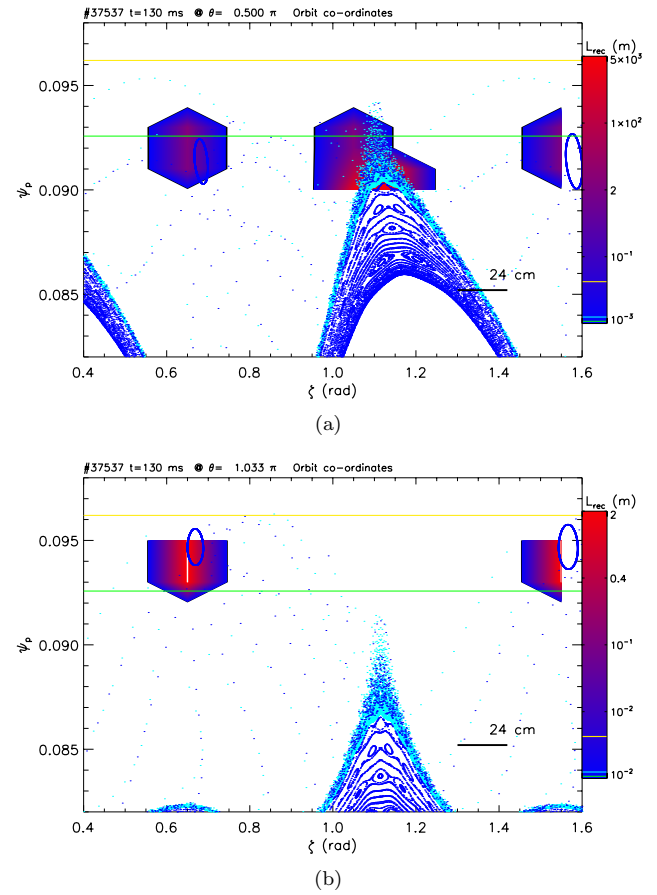


Figure 14. Poincaré recurrence length L_{rec} at two more poloidal angles, $\theta = 90^\circ$ (frame (a)) and 186° (frame (b)). This figure should be compared to the analog figure 7.

Finally, let us repeat the analysis at two different values of θ , namely $\theta = 90^\circ$ and 186° : results are shown in figures 14(a) and 14(b), respectively. At $\theta = 90^\circ$ the region of larger interaction remains the stochastic layer (~ 250 toroidal turns, $L_{rec} \sim 1.4 \div 3$ km), but the regions with the OP get closer to the wall. At $\theta = 186^\circ$ the plasma-wall interaction is completely governed by the $m = 0$ islands ($L_{rec} \sim 2.6 \div 3$ m), in all respects similar to what discussed in section 4.

6. Summary and conclusions

In this paper we discuss the role of toroidally coupled sidebands in determining the kinetic response of the plasma to an applied base mode of a well-defined helicity. The result is that sidebands are as important as the base mode in determining the details of plasma pressure and floating potential in the edge, when MPs are applied: this should be a caveat for tokamaks, since ELM stability depends directly on edge plasma pressure. Our case study is the topology of the RFX-mod helical edge ($r/a \gtrsim 0.85$), which is dominated by a $1/7$ modulation. In the past, this base mode was found to dominate measurements of electron pressure, floating potential and plasma flow [8–15]. New measurements show that $m = 0$ effects are strong [21, 22], the $0/7$ mode being the

main sideband toroidally coupled to the base mode [23]. This toroidal correction is found to be of order $\epsilon = a/R$. Simulations of magnetic topology and of connection lengths to the wall, performed with the guiding-center code ORBIT, reproduce in detail measurements, and provide an explanation of the observed deviation in terms of two structures that are well-known in chaos theory: a *stochastic layer* separating the 1/7 and 0/7 resonances, and *field line orbits* around the O-points of the 0/7 islands. Moreover, for the first time in plasma physics, a method based on the Poincaré recurrence time has been used, and confirms that the main structures determining transport in the edge region are the stochastic layer, with long recurrence times (>100 toroidal turns), and the O-points of the 0/7 islands, with shorter recurrences ($\tau_{\text{rec}} \sim 1$ toroidal turn). The large value of the recurrence time within the stochastic layer means that particles in this region experience a large plasma volume, before returning back, and this is consistent with the larger electron temperature measured in this region [21], in all respects similar to the tokamak ‘ergodic fingers’ [4]. The use of the Poincaré recurrence time is to be preferred with respect to the connection length, because it is an intrinsic property of the volume considered, and it does not depend e.g. on the starting and ending point of particle trajectories.

Results shown in this paper are in line with [59], where the importance of sidebands toroidally coupled with a base mode is demonstrated for a helical RFP and a circular tokamak, through an analytic, geometrical approach. These results should be of interest for the application of RMPs in tokamaks, as explained above: in this respect, while in the RFP and a circular tokamak toroidal coupling is limited to the Shafranov shift, only, in D-shaped tokamaks the effect should be even stronger, due to ellipticity and triangularity. In fact, recent similarity experiments with DIII-D performed on ASDEX-U [60] show that ELM suppression is achieved only with at least a moderate value of triangularity ($\delta > 0.25$). Our work shows that the kinetic plasma response to the same MP can be strongly different even with moderate values of toroidal coupling, since the spectrum of sidebands is significantly changed by toroidicity (compare the blue and red traces in figure 1).

Acknowledgments

The development of the Poincaré recurrence time calculation was done during a stay at the Princeton Plasma Physics Laboratory, in the frame of an international collaboration supported by EUROfusion within workpackage MST1. Our thank goes to Dr. Roberto Cavazzana for realizing the beautiful figure 10, and to the whole RFX team (in particular the head of operation Dr. Samuele Dal Bello) for continuous support. Last but not least, our thank goes to Giuliana Allen for carefully reading the manuscript. This work has received funding from the European Union’s Horizon 2020 research and innovation programme under grant agreement number 633053.

ORCID iDs

G. Spizzo  <https://orcid.org/0000-0001-8586-2168>
 M. Spolaore  <https://orcid.org/0000-0002-2350-2033>
 D. Terranova  <http://orcid.org/0000-0001-9339-283X>
 M. Veranda  <https://orcid.org/0000-0002-5821-2896>
 N. Vianello  <https://orcid.org/0000-0003-4401-5346>

References

- [1] Evans T.E. 2015 *Plasma Phys. Control. Fusion* **57** 123001
- [2] Evans T. et al 2008 *Nucl. Fusion* **48** 024002
- [3] Jakubowski M.W. et al and TEXTOR Team 2006 *Phys. Rev. Lett.* **96** 035004
- [4] Stoschus H., Schmitz O., Frerichs H., Reiser D., Jakubowski M., Unterberg B., Lehnen M., Reiter D., Samm U. and The TEXTOR Team 2012 *Nucl. Fusion* **52** 083002
- [5] Moyer R., Zeeland M.V., Orlov D., Wingen A., Evans T., Ferraro N., Hanson J., Nazikian R., Wade M. and Zeng L. 2012 *Nucl. Fusion* **52** 123019
- [6] Willensdorfer M. et al The ASDEX Upgrade Team and The EUROfusion MST1 Team 2016 *Plasma Phys. Control. Fusion* **58** 114004
- [7] White R.B. and Chance M.S. 1984 *Phys. Fluids* **27** 2455–67
- [8] Scarin P. et al and The RFX-mod Team 2011 *Nucl. Fusion* **51** 073002
- [9] Agostini M., Scaggion A., Scarin P., Spizzo G. and Vianello N. 2012 *Plasma Phys. Control. Fusion* **54** 065003
- [10] Vianello N. et al and The RFX-Mod Team 2013 *Nucl. Fusion* **53** 073025
- [11] De Masi G., Martines E., Spolaore M., Vianello N., Cavazzana R., Innocente P., Momo B., Spagnolo S. and Zuin M. 2013 *Nucl. Fusion* **53** 083026
- [12] Spizzo G. et al, RFX and TEXTOR Teams 2014 *Phys. Plasmas* **21** 056102
- [13] Vianello N. et al 2015 *Plasma Phys. Control. Fusion* **57** 014027
- [14] Spolaore M. et al 2015 *Nucl. Fusion* **55** 063041
- [15] Scarin P., Agostini M., Carraro L., Cavazzana R., Ciaccio G., De Masi G., Spizzo G., Spolaore M. and Vianello N. 2015 *J. Nucl. Mater.* **463** 467–70 (*Proc. 21st Int. Conf. on Plasma-Surface Interactions in Controlled Fusion Devices (Kanazawa, Japan May 26–30, 2014)*)
- [16] Evans T.E., Roeder R.K.W., Carter J.A. and Rapoport B.I. 2004 *Contrib. Plasma Phys.* **44** 235–40
- [17] Chen D., Zhu S., Zhang D. and Wang S. 2016 *Phys. Plasmas* **23** 054503
- [18] Rozhansky V., Kaveeva E., Molchanov P., Veselova I., Voskoboinikov S., Coster D., Kirk A., Lisgo S. and Nardon E. 2010 *Nucl. Fusion* **50** 034005
- [19] Gobbin M., Marrelli L. and White R.B. 2009 *Plasma Phys. Control. Fusion* **51** 065010
- [20] Ciaccio G., Schmitz O., Spizzo G., Abdullaev S.S., Evans T.E., Frerichs H. and White R.B. 2015 *Phys. Plasmas* **22** 102516
- [21] Agostini M. et al and The RFX-mod Team 2017 *Nucl. Fusion* **57** 076033
- [22] Scarin P., Agostini M., Carraro L., Spizzo G., Spolaore M. and Vianello N. 2017 *Nucl. Mater. Energy* (<https://doi.org/10.1016/j.nme.2017.03.006>)
- [23] Zanca P. and Terranova D. 2004 *Plasma Phys. Control. Fusion* **46** 1115
- [24] Ortolani S. and Schnack D. 1993 *Magnetohydrodynamics of Plasma Relaxation* (Singapore: World Scientific) p 39

- [25] Cappello S., Bonfiglio D., Escande D.F., Guo S.C., Alfier A., Lorenzini R. and The RFX Team 2008 *AIP Conf. Proc.* **1069** 27–39
- [26] Sonato P. et al 2003 *Fusion Eng. Des.* **66–8** 161–8 *Proc. 22nd Symp. on Fusion Technology, (Helsinki Finland, 9–13 September 2002)*
- [27] Marrelli L. et al 2007 *Plasma Phys. Control. Fusion* **49** B359–69
- [28] Puiatti M.E. et al 2015 *Nucl. Fusion* **55** 104012
- [29] White R.B. 2013 *Phys. Plasmas* **20** 022105
- [30] White R.B. 2013 *Phys. Plasmas* **20** 042116
- [31] Ciaccio G., Veranda M., Bonfiglio D., Cappello S., Spizzo G., Chacon L. and White R.B. 2013 *Phys. Plasmas* **20** 062505
- [32] Spizzo G., Franz P., Marrelli L. and Martin P. 2001 *Plasma Phys. Control. Fusion* **43** L17
- [33] Schmitz O. et al and The TEXTOR. Team 2008 *Nucl. Fusion* **48** 024009
- [34] Callen J., Hegna C. and Cole A. 2013 *Nucl. Fusion* **53** 113015
- [35] Spizzo G., Cappello S., Cravotta A., Escande D.F., Predebon I., Marrelli L., Martin P. and White R.B. 2006 *Phys. Rev. Lett.* **96** 025001
- [36] Martinez E., Lorenzini R., Momo B., Munaretto S., Innocente P. and Spolaore M. 2010 *Nucl. Fusion* **50** 035014
- [37] Agostini M., Scarin P., Cavazzana R., Carraro L., Grando L., Taliercio C., Franchin L. and Tiso A. 2015 *Rev. Sci. Instrum.* **86** 123513
- [38] Spizzo G., White R.B. and Cappello S. 2007 *Phys. Plasmas* **14** 102310
- [39] Rubino G., Borgogno D., Veranda M., Bonfiglio D., Cappello S. and Grasso D. 2015 *Plasma Phys. Control. Fusion* **57** 085004
- [40] Lichtenberg A.J. and Leiberman M.A. 1992 *Regular and Chaotic Dynamics* 2nd edn (New York, USA: Springer) p 51
- [41] Fitzpatrick R. 2016 *Phys. Plasmas* **23** 122502
- [42] White R.B. 2014 *The Theory of Toroidally Confined Plasmas* 3rd edn (London: Imperial College Press) pp 238–40
- [43] White R.B. 2014 *The Theory of Toroidally Confined Plasmas* 3rd edn (London: Imperial College Press) p 15
- [44] Nguyen F., Ghendrih P. and Grosman A. 1997 *Nucl. Fusion* **37** 743
- [45] Kirk A. et al and the MAST. Team 2013 *Nucl. Fusion* **53** 043007
- [46] Ciaccio G., Schmitz O., Abdullaev S., Frerichs H., Agostini M., Scarin P., Spizzo G., Vianello N. and White R.B. 2014 *Nucl. Fusion* **54** 064008
- [47] Schmitz O. et al 2009 *J. Nucl. Mater.* **390–1** 330–4 (*Proc. 18th Int. Conf. on Plasma-Surface Interactions in Controlled Fusion Devices (Toledo, Spain, 26–30 May 2008)*)
- [48] Serianni G., Baker W. and Dal Bello S. 2003 *Rev. Sci. Instrum.* **74** 1558–62 (papers from the *14th Topical Conf. on High Temperature Plasma Diagnostics*)
- [49] Zaslavsky G. M 2005 *Hamiltonian Chaos and Fractional Dynamics* (Oxford: Oxford University Press) ch 11, pp 173–86
- [50] Eckmann J.P., Kamphorst S.O. and Ruelle D. 1987 *Europhys. Lett.* **4** 973
- [51] Viana R.L., Toufen D.L., Guimarães-Filho Z.O., Caldas I.L., Gentle K.W. and Nascimento I.C. 2016 *Recurrence Analysis of Turbulent Fluctuations in Magnetically Confined Plasmas* (Cham: Springer) pp 341–53
- [52] Boltzmann L. 1896 *Ann. Phys.* **293** 773–84
- [53] White R.B., Benkadda S., Kassibrakis S. and Zaslavsky G.M. 1998 *Chaos* **8** 757–67
- [54] Zaslavsky G.M. 2005 *Hamiltonian Chaos and Fractional Dynamics* (Oxford: Oxford University Press) ch 12, pp 187–99
- [55] D'Angelo F. and Paccagnella R. 1996 *Phys. Plasmas* **3** 2353–64
- [56] Spizzo G., White R.B., Cappello S. and Marrelli L. 2009 *Plasma Phys. Control. Fusion* **51** 124026
- [57] Rechester A.B. and Rosenbluth M.N. 1978 *Phys. Rev. Lett.* **40** 38–41
- [58] Sanchez R. and Newman D.E. 2015 *Plasma Phys. Control. Fusion* **57** 123002
- [59] Predebon I., Momo B., Terranova D. and Innocente P. 2016 *Phys. Plasmas* **23** 092508
- [60] Nazikian R., Suttrop W., Kirk A., Evans T.E., Grierson B.A., McDermott R., Paz-Soldan C., Orlov D. and Willensdorfer M. 2016 First Observation of ELM Suppression in ASDEX-Upgrade In A Similarity Experiment With DIII-D *Preprint: 2016 IAEA Fusion Energy Conference, Kyoto, Japan, 17–22 October 2016* (<https://conferences.iaea.org/indico/event/98/session/12/contribution/952>)